JOURNAL OF GEOPHYSICAL RESEARCH: ATMOSPHERES, VOL. 118, 4280–4289, doi:10.1002/jgrd.50391, 2013

A link between tropical intraseasonal variability and Arctic stratospheric ozone

King-Fai Li,[1] Baijun Tian,[2] Ka-Kit Tung,[3] Le Kuai,[2] John R. Worden,[2] Yuk L. Yung,[1] and Benjiman L. Slawski[1]

Received 25 August 2012; revised 3 April 2013; accepted 4 April 2013; published 28 May 2013.

[1] Previous studies using satellite measurements showed evidence that subtropical upper troposphere/lower stratosphere ozone (O_3) can be modulated by tropical intraseasonal variability, the most dominant form of which is the Madden Julian Oscillation (MJO) with a period of 30–60 days. Here we further study the MJO modulation in the upper troposphere/lower stratosphere O_3 over the northern extratropics and the Arctic. Significant MJO-related O_3 signals (13–20 Dobson units) are found over the northern extratropics (north of 30°N). The O_3 anomalies change their magnitude and patterns depending on the phase of the MJO. Over the Arctic, the MJO-related O_3 anomalies are dominated by a wave number 2 structure and are anticorrelated with the geopotential height (GPH) anomalies at 250 hPa. The latter is similar to the findings in the previous studies over subtropics and indicates that the Arctic upper troposphere/lower stratosphere O_3 anomalies are associated with dynamical motions near the tropopause. The teleconnection from the tropics to the Arctic is likely through propagation of planetary waves generated by the equatorial heating that affects the tropopause height and O_3 at high latitudes.

Citation: Li, K.-F., B. Tian, K.-K. Tung, L. Kuai, J. R. Worden, Y. L. Yung, and B. L. Slawski (2013), A link between tropical intraseasonal variability and Arctic stratospheric ozone, *J. Geophys. Res. Atmos.*, *118*, 4280–4289, doi:10.1002/jgrd.50391.

1. Introduction

[2] The Madden-Julian Oscillation (MJO) is the dominant form of intraseasonal variability (30–60 days) in the tropical atmosphere, especially during the boreal winter (November–April) [*Madden and Julian*, 1971, 1972; *Zhang*, 2005; *Lau and Waliser*, 2011]. A typical boreal winter MJO event starts with a convective disturbance over the far western equatorial Indian Ocean, and then, it intensifies and propagates eastward slowly (~5 m s^{-1}) to the central equatorial Pacific Ocean. In the equatorial Indian and West Pacific Oceans, where the sea surface temperature (SST) is relatively warm, the MJO convective disturbance interacts strongly with the upper level atmospheric flow, cloud field, surface winds, and heat fluxes. Once the MJO convective disturbance reaches the date line, and thus cooler SSTs, it subsides, and the MJO is largely confined to the upper tropospheric wind field anomalies. During the boreal summer, the change in the large-scale circulation associated with the Asian summer monsoon results in the MJO disturbances propagating northeastward. In this paper, we are interested in the boreal winter MJO only.

[3] Increasing number of studies have used satellite data to characterize the impact of the MJO on atmospheric species [*Tian and Waliser*, 2011], such as water vapor [*Tian et al*., 2006; *Wong and Dessler*, 2007; *Tian et al*., 2010], carbon dioxide [*Li et al*., 2010], ozone (O_3) [*Fujiwara et al*., 1998; *Ziemke and Chandra*, 2003; *Tian et al*., 2007; *Liu et al*., 2009; *Weare*, 2010; *Li et al*., 2012], carbon monoxide [*Wong and Dessler*, 2007], aerosols [*Tian et al*., 2008, 2011], as well as nitrogen dioxide generated from lightning [*Virts et al*., 2011]. These findings are useful for improving air quality forecasts to weekly/monthly timescales, which help warn the public in advance and help authorities to take appropriate actions [*Hollingsworth et al*., 2008].

[4] The MJO modulations in O_3 have been observed in both the troposphere [*Ziemke and Chandra*, 2003; *Ziemke et al*., 2007] and the upper troposhere/lower stratosphere [*Tian et al*., 2007; *Li et al*., 2012], the latter being more intriguing because of the possibility of teleconnection to high latitudes. Using the total column O_3 data observed from space by the Total Ozone Mapping Spectrometer (TOMS) and the Atmospheric Infrared Sounder, *Tian et al*. [2007] found that the largest signal [5–10 Dobson units (DU)] of the MJO modulation in the total column ozone (X_{O_3}) anomaly is in the subtropics over the Indo-Pacific and the eastern Pacific regions, despite the fact that the MJO convective disturbance is mostly an equatorial phenonmon. Subtropical negative X_{O_3} anomalies flank or lie to the west of equatorial enhanced MJO convection and propagate slowly eastward

[1]Division of Geological and Planetary Sciences, California Institute of Technology, Pasadena, California, USA.
[2]Jet Propulsion Laboratory, California Institute of Technology, Pasadena, California, USA.
[3]Department of Applied Mathematics, University of Washington, Seattle, Washington, USA.

Corresponding author: K.-F. Li, Division of Geological and Planetary Sciences, California Institute of Technology, Pasadena, CA, USA. (kfl@gps.caltech.edu)

2169-897X/13/10.1002/jgrd.50391

with the equatorial MJO convective disturbance. These negative X_{O_3} anomalies are typically collocated with subtropical upper tropospheric anticyclones and are anticorrelated with positive geopotential height (GPH) anomalies near the tropopause. The same anticorrelation also applies to positive subtropical X_{O_3} anomalies, subtropical upper tropospheric cyclones, and negative GPH anomalies near the tropopause. This suggests that the majority of the MJO signal in X_{O_3} is likely driven by the vertical movement of the subtropical tropopause induced by anomalous equatorial heating during the MJO cycle [*Kiladis et al*., 2001]. This anticipated mechanism is supported by a recent study [*Li et al*., 2012] using vertically resolved satellite O_3 data measured by the Microwave Limb Sounder (MLS) [*Waters et al*., 2006], the Tropospheric Emission Spectrometer (TES) [*Beer*, 2006], and the Ozone Monitoring Instrument (OMI) [*Levelt et al*., 2006a]. That study showed that at least ~70% of the observed MJO-related anomalies in X_{O_3} can be explained by the corresponding anomalies of the partial column O_3 in the lower stratosphere and the upper troposphere between 30 and 200 hPa. Some evidence of the stratospheric MJO signal in the O_3 concentration has been also found from reanalysis data [*Weare*, 2010].

[5] Both *Tian et al*. [2007] and *Li et al*. [2012] limited their discussions to tropics and subtropics (±40°). Whether the MJO can impact the O_3 over extratropics or polar regions is still unknown. It has been shown that extratropical weather may be linked to tropical convection through the large-scale overturning circulation anomalies associated with the tropical convection [*Egger and Weickmann*, 2007; *Weickmann and Berry*, 2009] and Rossby wave trains that extend eastward and poleward across the midlatitudes [*Jin and Hoskins*, 1995]. Conversely, tropical convection may be also modified by extratropical waves [*Hoskins and Yang*, 2000]. It is also known that the MJO influence on extratropical dynamics and weather [*Kim et al*., 2006; *Pan and Li*, 2008; *Yoo et al*., 2011, 2012] is one of the major sources of predictability in the extratropics on the intraseasonal time scales during the wintertime [*Jones et al*., 2004; *Jung et al*., 2010; *Lin et al*., 2010a, 2010b; *Vitart and Molteni*, 2010]. The associations between the tropical and extratropical patterns frequently express themselves as global teleconnection patterns [*Ferranti et al*., 1990; *Cassou*, 2008; *Roundy and Gribble-Verhagen*, 2010]. Anomalous extratropical flows can be forced by tropical vorticity perturbations resulting from adiabatic heatings during the MJO cycle [*Ferranti et al*., 1990; *Weare et al*., 2012]. The extratropical response in the GPH during the boreal winter is dominated by anomalous circulation at ~60°N. Some studies suggest that the circulation patterns of the GPH anomalies may correlate with the Pacific–North American (PNA) pattern [*Wallace and Gutzler*, 1981; *Mori and Watanabe*, 2008] and North Atlantic Oscillation [*Cassou*, 2008; *Lin et al*., 2009]. For a review of the MJO teleconnection, please see *Lau and Waliser* [2011, chap. 14].

[6] The aim of the present work is to extend the studies of *Tian et al*. [2007] and *Li et al*. [2012] to provide the MJO-related pattern of O_3 in the northern extratropics and Arctic during boreal (northern) winter. We will show that the extratropical response in the GPH to the equatorial MJO also leads to intraseasonal variations of extratropical and polar O_3. Section 2 describes the data used and the statistical methods for examining the MJO signal in Arctic O_3. Section 3 describes the results, followed by discussions and a brief summary in section 4 on the mechanism connecting the Arctic O_3 to the tropical MJO disturbances.

2. Data and Methods

[7] Details of MLS, TES, and OMI O_3 data can be found in *Li et al*. [2012]. In this work, we update these data with recent observations. For MLS, we use the Level-2 v3.3 O_3 product [*Livesey et al*., 2011] from 1 November 1 2004 to 18 December 2011. The MLS O_3 have been retrieved every 165 km along the suborbital track on six levels per decade of pressure from 215 hPa through the stratosphere, with an effective horizontal resolution of ~300 km × 6 km and an effective vertical resolution of ~3 km in the upper troposphere. For TES, we use the Level-2 O_3 product [*Beer et al*., 2001; *Jourdain et al*., 2007; *Worden et al*., 2007] from 1 November 2004 to 31 December 2010. The TES O_3 products have been retrieved on 67 pressure levels between the surface and 5 hPa, with an effective horizontal resolution of 5.3 km × 8.5 km and an effective vertical resolution of ~6 km for clear-sky conditions. TES makes one observation every ~100 km along the orbit. The TES data have been shown by *Boxe et al*. [2010] to be able to capture the upper tropospheric and stratospheric Arctic ozone variability; however, they have little sensitivity to lower tropospheric O_3 variations due to low thermal contrast and clouds [*Kulawik et al*., 2006; *Worden et al*., 2007; *Eldering et al*., 2008]. For OMI, we use the Level-3 product [*Levelt et al*., 2006b] from 1 November 1, 2004 to 30 November 2011, which were recently validated by *Kroon et al*. [2011] and shown to be able to capture stratospheric O_3 variability globally. The retrieved OMI O_3 has an effective horizontal resolution of 13 km × 24 km. Since OMI estimates O_3 concentrations from the backscattered solar radiation, no data are provided during Arctic polar nights (December–February) for latitudes north of 70°N. All of the MLS, TES, and OMI O_3 products are regridded into 5° longitude × 4° latitude. Typical uncertainties of individual O_3 retrievals from nadir/limb scans are 1%–2%. Because of composite averaging upon 20–120 individual soundings in each MJO phase, the uncertainties of the resultant MJO patterns are much better than 1%–2% (see next section).

[8] To evaluate the robustness of the spaceborne measurements, the ground-based O_3 column data archived in World Ozone and Ultraviolet Radiation Data Center (WOUDC) will be also examined. In this study, only those WOUDC stations that provide O_3 data during 2001–2010 would be used. In addition, to examine any long-term changes in the MJO-related O_3 patterns obtained from the above data sets, the Level-3 version 8 Total Ozone Mapping Spectrometer (TOMS) total column O_3 (TCO) data from 1 November 1978 to 14 December 2005 will be also used. The TOMS Level-3 O_3 data have a horizontal resolution of 1.25° longitude × 1° latitude. Same as OMI, TOMS measured TCO from the backscattered solar radiation, and no data are provided during Arctic polar nights for latitudes north of 70°N.

[9] Rainfall data (1 November 2002 to 28 Februrary 2010) from the Tropical Rainfall Measuring Mission (TRMM) 3B42 product [*Huffman et al*., 2007] are used to trace the movement of the MJO-related equatorial convective

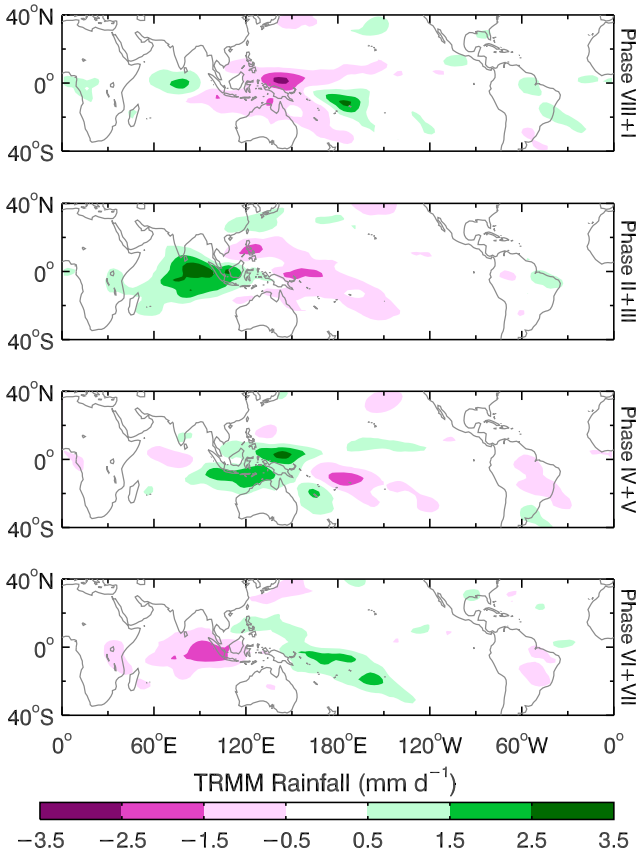

Figure 1. The movement of the MJO disturbance in the tropics depicted by rainfall anomalies over the eight MJO phases defined by the Real-Time Multivariate MJO (RMM) index. For simplicity, the eight phases are further reduced to four phases by combining Phases 8 and 1, 2 and 3, 4 and 5, and 6 and 7.

anomalies. The 8 times daily TRMM 3B42 rainfall data have a horizontal resolution of 0.25° longitude × 0.25° latitude. The 4 times daily GPH (1 November 2002 to 30 November 2011) data from the European Centre for Medium-Range Weather Forecasting (ECMWF) Re-Analysis Interim project [*Dee et al.*, 2011] have a horizontal resolution 1.5° longitude × 1.5° latitude and are used to trace the tropopause movement.

[10] As in *Li et al.* [2012], all time series are first deseasonalized, and a running-average band-pass filter for 15–90 days is applied to the time series. To identify MJO events for a composite analysis, the all-season Real-Time Multivariate MJO (RMM) daily index [*Wheeler and Hendon*, 2004] which characterizes the state of the MJO in terms of its amplitude and phase is used. According to the RMM index, a MJO cycle (typically ~40–60 days) is divided into eight phases, each roughly lasting ~5–7 days. Phase 1 represents developing positive rainfall anomalies in the western equatorial Indian Ocean. These positive rainfall anomalies travel eastward to the equatorial Indian Ocean during Phases 2 and 3. They then reach the Maritime Continents in Phases 4 and 5 and further to the western equatorial Pacific in Phases 6 and 7. These positive rainfall anomalies are weakened when they reach the central equatorial Pacific in Phase 8, marking the end of a MJO cycle [*Hendon and Salby*, 1994; *Waliser et al.*, 2009]. Composite MJO cycles of relevant quantities (rainfall, O_3, and GPH) are produced by separately averaging together all daily values of the given quantity for each phase of the MJO, considering only strong amplitude events where $RMM_1^2 + RMM_2^2 \geq 1$. As an example, the MJO composites of the TRMM rainfall are shown in Figure 1. For simplicity, the eight typical phases defined by the RMM index have been reduced to four by summing Phases 8 and 1 (VIII + I), 2 and 3 (II + III), 4 and 5 (IV + V), and, finally, 6 and 7 (VI + VII).

[11] During the boreal winters of November 2004 to April 2011 when the MLS and OMI O_3 measurements are used in this work, there are ~19 strong MJO events, which constitute 74–121 days in each of the eight phases [cf. *Li et al.*, 2012, Figure 1]. As a result, a total of 50–120 MLS and OMI soundings are averaged in the grid boxes for each phase [cf. *Li et al.*, 2012, Figure 2a]. Similarly, during the boreal winters of November 2004 to December 2010 when the TES O_3 measurements are used in this work, there are ~18 strong MJO events, which constitute 58–110 days in each of the eight phases. Because TES has much lower horizontal resolution, only a total of 20–40 TES soundings are averaged in the grid boxes for each phase [cf. *Li et al.*, 2012, Figure 2b].

[12] The uncertainties of the MJO composites can be estimated by the term $\alpha\sigma/\sqrt{N}$, where σ and N are the standard deviation and the effective number of data samples being averaged, respectively, in each MJO phase and in each grid box, and α is the critical value of the t distribution for a two-sided 95% confidence level. N is the total number of data samples being averaged divided by the correlation time scale, which is derived from the lag correlation [*Leith*, 1973] and is ~15 days (the lower bound of our band-pass filter). As a result, the uncertainties of the MJO signals are less than 1.2 DU for TES PCO and OMI TCO, 0.4 DU for MLS PCO and TOMS TCO, 1 mm d^{-1} for TRMM rainfall, and 7 m for GPH_{250}.

3. Results

3.1. Climatological Mean Profile

[13] Before describing the MJO patterns, it is informative to show the climatological mean O_3 profiles averaged over the Arctic. In Figure 2, the solid line represents the boreal winter mean O_3 profiles in the latitude band 60°N–80°N. The latitude band 80°N–90°N may contain missing data during Arctic winters, so these latitudes are not included in the average. The combination of MLS (blue) and TES (green) provides the whole O_3 profile from ground to upper stratosphere (only 1–1000 hPa is shown). Here for ease of comparison with the partial columns shown in Figures 2 and 3, we adopt a unit DU/km for the O_3 concentration, which is equivalent to 2.69×10^{11} molecules/cm^3. Over the Arctic, the O_3 concentration peaks at ~60 hPa (20 km) with a peak value of ~20 DU/km. The O_3 concentration drops to less than 10 DU/km below 200 hPa and above 20 hPa. At 250 hPa, O_3 increases as altitude increases. As will be shown below (section 3.3), these slopes determine the sign of correlation between GPH and O_3 anomalies over the MJO life cycle.

3.2. MJO Patterns in the Northern Hemisphere

[14] Figures 3 shows the northern hemispheric spatiotemporal patterns in MJO-related partial column O_3 (PCO)

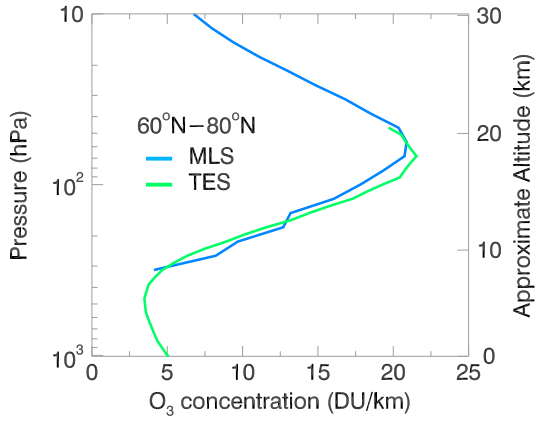

Figure 2. The mean ozone (O_3) profile over the Arctic (60°N–80°N) during boreal winter (November–April) observed by (blue) MLS and (green) TES. O_3 concentrations are expressed in DU/km, which is equivalent to 2.69×10^{11} molecules/cm^3. Note that near 250 hPa, O_3 increases with altitude.

anomalies derived from MLS (for 42–316 hPa) and TES (for 42–316 hPa) and TCO anomalies derived from OMI. A 25° longitude × 12° latitude spatial smoothing has been applied to these MJO-related patterns. Note that the altitude difference between the pressure layers 42 and 316 hPa is ~10 km and is greater than the vertical resolutions of MLS and TES O_3 retrievals. The integrations of PCO between these two layers thus ensure that the impacts of MLS and TES O_3 vertical resolutions on the horizontal patterns would be minimized. *Li et al*. [2012] compared the PCO and TCO anomalies with GPH at 150 hPa (hereafter GPH_p denotes for the pressure level at p hPa), which is approximately the height of the tropical tropopause. However, for high latitudes, GPH_{250} is more appropriate [*Hoinka*, 1998]. Therefore, we overlay the GPH_{250} anomaly (black solid/dotted lines) in the figures. Also shown are the rainfall anomalies (purple/green solid lines). Note that anticlockwise orientation is from west to east. Africa is located at the top of the azimuth projection (0°), the southeastern Asia is located at the lower left-hand corner (120°E), and the eastern Pacific is located at the lower right corner (120°W). The overall MJO patterns of O_3 are dominated by wave number 2 and 3 structures around the North Pole. The details in individual phases are described as follows.

[15] During Phase VIII + I, positive equatorial rainfall anomalies related to the MJO is found in the western Indian Ocean. There is also negative equatorial rainfall anomalies extending from the east of the Maritime Continents to the western Pacific Ocean. For MLS (Figure 3a), the Arctic PCO O_3 anomaly is dominated by a dumbbell-like negative pattern, which extends from Alaska (−8 DU), crossing the North Pole (−2 DU), to Russia (−4 DU). This negative pattern is surrounded by a positive anomaly, which extends from Europe (4 DU), going eastward along the 30°N latitude circle (2 DU), to the center of action (COA) in the northern Pacific (8 DU). There is also a positive anomaly (4 DU) over the eastern U.S. These MLS O_3 anomalies are well anticorrelated with the GPH_{250} anomalies. Note that while the rainfall anomalies are confined in the Eastern Hemisphere, the Arctic PCO and GPH anomalies are significant over both Eastern and Western Hemispheres. The alternating positive and negative anomalies around the great circle near 60°N form a wave number 2/wave number 3 structure.

[16] In Phase II + III, the rainfall anomalies has moved eastward by ~30°. The MLS PCO anomalies are dominated by a positive pattern (3 DU) that covers Alaska and Siberia, which further extends over the North Pole (2 DU) and covers part of the northern Atlantic and Russia. This positive anomaly is surrounded by a weak negative anomaly (2–4 DU) that extends from the eastern U.S., going eastward along the 30°N latitude circle, to the northern Pacific COA. Again, these O_3 anomalies are well anticorrelated with the GPH_{250} anomalies. Phase IV + V is simply characterized by reversed signs in rainfall, GPH_{150}, and MLS PCO anomalies with respect to Phase VIII + I. Finally, Phase VI + VII is characterized by a few weak positive and negative anomalies (<2 DU) over the northern extratropics.

[17] Overall, the correlation coefficient between the MLS PCO and GPH_{250} anomalies in all MJO phases for latitudes northward of 45°N is −0.78 (>99% confidence level; Table 1). Since the O_3 concentration increases with altitude near 250 hPa (cf. Figure 2), the negative correlation suggests that the MJO-related PCO variability over the Arctic region is likely associated with the tropopause displacements caused by equatorial heating related to MJO [*Ferranti et al*., 1990], similar to the findings in previous studies over subtropics [*Tian et al*., 2007; *Li et al*., 2012].

[18] The robustness of the anticorrelation between the MLS PCO and GPH_{250} anomalies is supported by independent O_3 measurements from TES. The MJO-related patterns for TES PCO (Figure 3b) are very similar to those of MLS (Figure 3a). The correlation coefficient between the TES PCO and GPH_{250} anomalies for latitudes north of 45°N is −0.59 (>99% confidence level), which is less than that for MLS (Table 1).

[19] Similar MJO patterns are also seen from OMI TCO measurements (Figure 2c). The correlation coefficient between the OMI TCO and GPH_{250} anomalies for latitudes north of 45°N is −0.59 (>99% confidence level; Table 1). There are small signals (~1 DU) in the tropical regions observed by OMI that are absent from MLS and TES, which are likely from the troposphere [*Ziemke and Chandra*, 2003; *Tian et al*., 2007]. There are also large signals (~10 DU) north of Siberia near the Arctic observed by OMI in Phase VI + VII. However, because of the absence of observations during polar nights (December–February), the observed large signals near the Arctic by OMI may not be robust (cf. section 3.4).

[20] The MLS PCO are well correlated with TES PCO (correlation coefficient 0.78 with a >99% confidence level) and OMI TCO (correlation coefficient 0.76 with a >99% confidence level; Table 1). TES PCO and OMI TCO are also correlated but with a smaller correlation coefficient of 0.59 (>99% confidence level), likely because these instruments are sensitive to O_3 in different parts of the atmosphere (i.e., TES for troposphere and OMI for the whole atmosphere).

3.3. Vertical Structures

[21] *Li et al*. [2012] showed that for the vertical structures of eastward propagating O_3 anomalies in subtropical regions (14°N–34°N and 14°S–34°S) during the MJO life cycle derived from MLS and TES observations, the subtropical

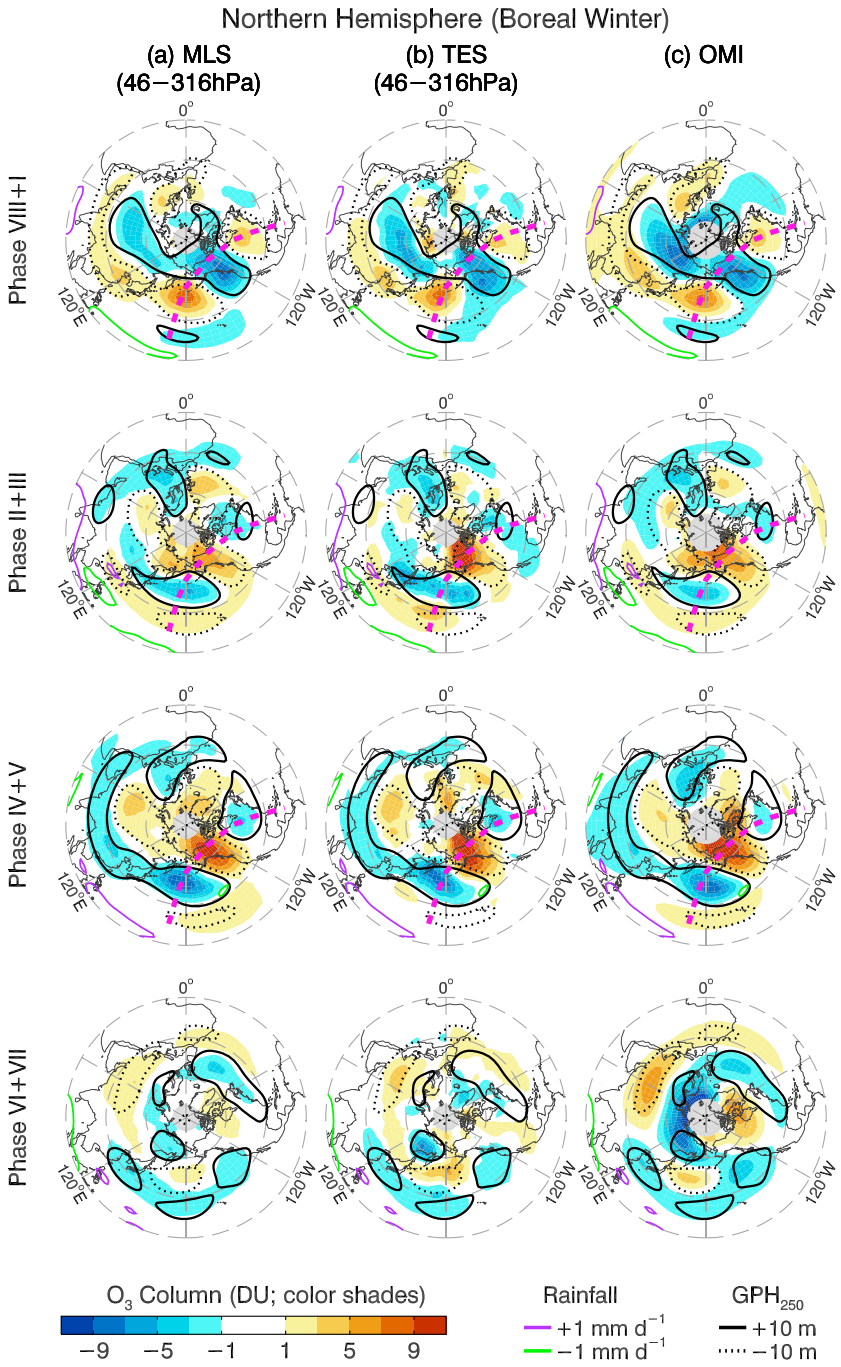

Figure 3. The Madden-Julian Oscillation (MJO) modulations in (a) MLS partial column O_3 (PCO), (b) TES PCO, and (c) OMI total column O_3 (TCO) for Northern Hemisphere. Also overlaid are rainfall anomalies from TRMM (green/purple) and geopotential height (GPH) anomalies at 250 hPa (GPH_{250}) from ECMWF interim reanalysis (dotted/solid). The shaded area represents O_3 column in Dobson units. The pink dashed line in the top left panel highlights the Rossby wave train that may be associated with the Pacific-North America (PNA) pattern.

MJO signals are mainly from the layer in the upper troposphere and the lower stratosphere. Such analysis turns out to be very useful for diagnosing possible dynamical causes. Here we replot their vertical structures in the sub-Arctic region (60°N–80°N) in Figure 3. The equatorial rainfall anomalies (solid) averaged over ±5° latitudes) are used to illustrate the propagation of the MJO convective disturbances, which propagates from the equatorial Indian Ocean to the equatorial central Pacific throughout the MJO life cycle, as discussed previously. The GPH_{250} anomalies (dashed) averaged over 60°N–80°N are also overlaid.

[22] The MLS O_3 anomalies (Figure 4a) are most prominent near the northern Pacific COA (130°W) at 130 hPa, with an amplitude ±1 DU/km. In Phase VIII + I, a negative MLS upper troposphere/lower stratosphere partial column O_3 anomaly (−0.8 DU/km) is developed near the

Table 1. Correlation Coefficients of the MJO-Related Anomalies of Geopotential Height at 250 hPa (GPH_{250}) With Those of MLS Partial Column Ozone (PCO), TES PCO, and OMI Total Column Ozone (TCO) for Latitudes Poleward of 45°N[a]

Correlation Coefficient	Arctic GPH_{250}	MLS PCO	TES PCO	OMI TCO
MLS PCO	−0.78	1		
TES PCO	−0.59	0.78	1	
OMI TCO	−0.59	0.76	0.59	1

[a]The correlation coefficients among the MLS PCO, TES PCO, and OMI TCO are also shown. A *t* test suggests that the confidence levels of these correlation coefficients are better than 99%.

northern Pacific COA, which becomes positive (0.8 DU/km) in the subsequent Phases II + III and IV + V. Finally, in Phase VI + VII, the anomaly near the northern Pacific COA becomes negative again (−0.3 DU/km). The TES O_3 anomalies evolve similarly during the MJO life cycle (Figure 4b), but we note that the MJO-related amplitude is larger (ranged from −0.8 to 1.6 DU/km). Because the horizontal resolution of MLS O_3 is much coarser than that of TES O_3, the spatiotemporal patterns and, thus, the MJO-related amplitudes obtained from MLS O_3 are expected to be smoother that those obtained from TES O_3. The GPH_{150} anomalies exhibit the largest amplitude (±50 m) near the northern Pacific COA and are anticorrelated with the O_3 anomalies, as discussed above.

3.4. WOUDC O_3

[23] Daily ground-based TCO measurements from the WOUDC network provide independent data sets for evaluating the robustness of the MJO-related O_3 patterns obtained above. There are total 225 WOUDC stations in the Northern Hemisphere (orange and blue dots in Figure 5a). We adopt the following quality controls on the WOUDC station data: (A) Only those stations where more than two thirds of the total number of days during 2001–2010 had O_3 observations will be included in the analysis; and (B) define seasonal anomalies as the difference between the daily O_3 values and the mean annual cycle; if an absolute seasonal anomaly is greater than 3 times the standard deviation of all the seasonal anomalies, then the corresponding daily O_3 measurements will be ignored. Fifty-eight stations in the Northern Hemisphere satisfy Criterion A, most of which are located over Europe (blue dots in Figure 5a).

[24] To further enhance the signal-to-noise ratio, we average the WOUDC O_3 data at two selected regions (Figures 5b and 5c): one over Europe (15°W–30°E, 35°N–70°N; Box 1 in Figure 5a) and one over Japan (125°E–144°E, 23°N–48°N; Box 2 in Figure 5a). Twenty-one and six WOUDC stations have been included in the average over Europe and Japan, respectively. Table 2 lists the identification numbers of the

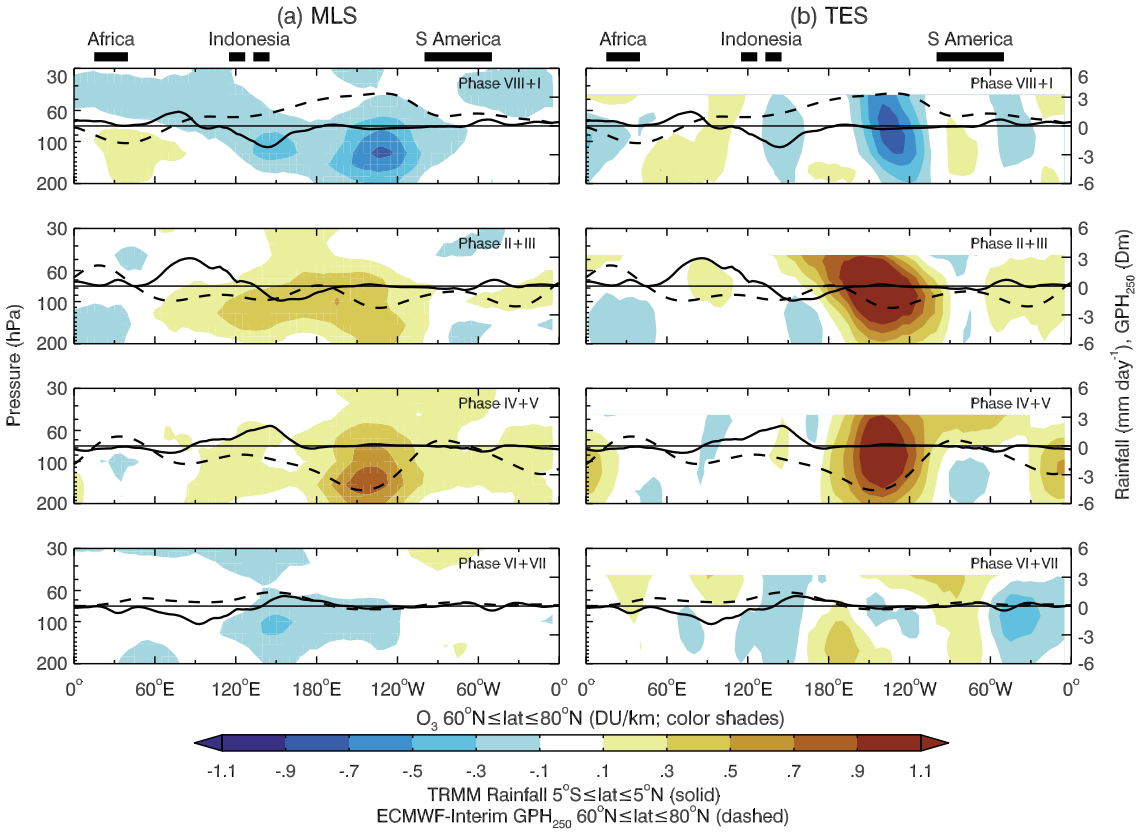

Figure 4. Zonal propagation of the MJO signal in O_3 concentrations along the subarctic latitude band 60°N–80°N. (solid lines) Equatorial rainfall anomalies averaged over latitudes within ±5°. (dashed lines) GPH_{250} averaged over 60°N–80°N. The GPH_{250} anomalies are expressed in decameters (1 Dm = 10 m).

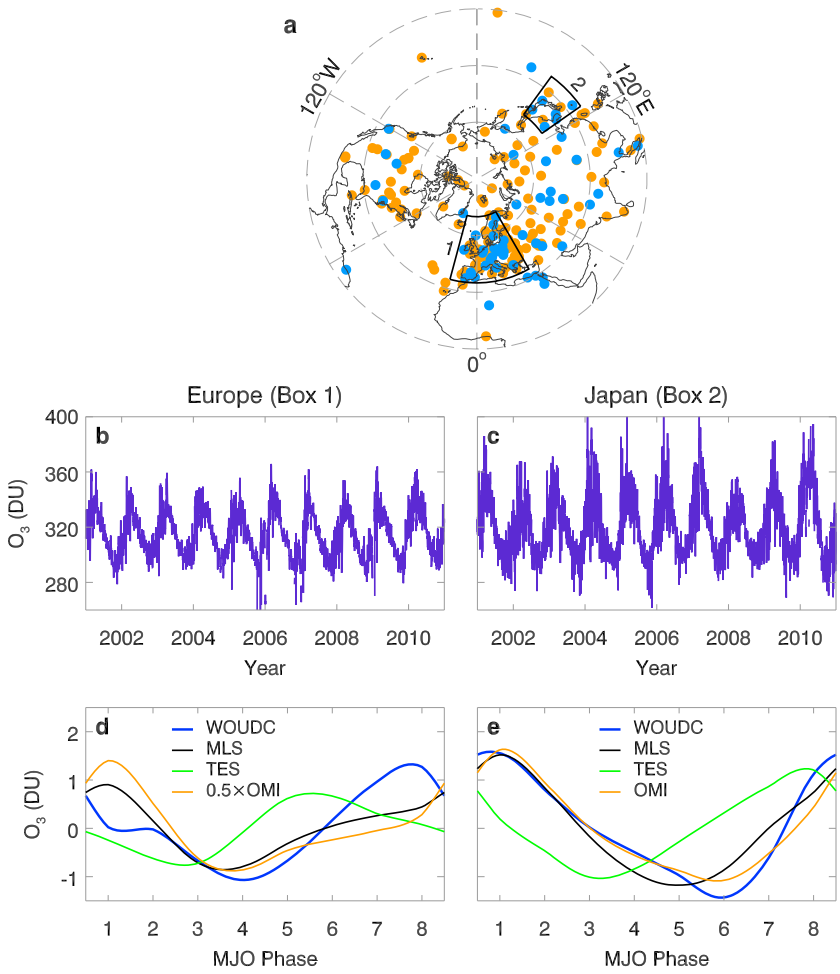

Figure 5. MJO analysis on WOUDC O_3 data. (a) Distribution of all (orange and blue dots) WOUDC stations. The blue dots represent stations that had O_3 observations during 2001–2010. (b, c) Average time series over Box 1 (Europe) and Box 2 (Japan) defined in Figure 5a. (d, e) MJO composites of (blue line) WOUDC TCO, (black line) MLS PCO, (green line) TES PCO, and (orange line) OMI TCO over Boxes 1 and 2. Note that in Figure 5d, the OMI TCO has been scaled by a factor of 0.5.

selected stations. The MJO-composite average of these time series are obtained by removing the mean annual cycles, applying the 15–91 day band-pass filter, and averaging over the MJO phases defined by the RMM index. The MJO-related time series of O_3 observed from MLS, TES, and OMI are also averaged over these regions for comparison, which are shown in Figures 5d and 5e.

[25] Over Europe (Figure 5d), the MJO time series derived from MLS PCO (black line), OMI TCO (orange line), and WOUDC TCO (purple line) observations covary closely in-phase, except that the MJO amplitude of the OMI time series is twice the other two. The WOUDC TCO and MLS PCO anomalies attain minima of −1 DU at around Phase 4 and maxima of +1 DU at around Phase 1. The agreement between MLS PCO and WOUDC TCO implies that the MJO-related signals in extratropical O_3 are dominated by lower stratospheric variation. On the other hand, given that both WOUDC and OMI measurements are sensitive to TCO, the relatively large MJO amplitude observed by OMI may be an artifact due to the lack of data during Arctic polar nights. Furthermore, the MJO-related time series derived from TES PCO (green line) shows an MJO amplitude similar to those of MLS PCO and WOUDC TCO, but there is a phase lead of ~1–2 MJO phases by TES PCO, i.e. ~5–10 days, compared to the other three, including OMI TCO. As TES is more sensitive to the tropospheric column, this phase lead relative to the MLS, OMI, and WOUDC measurements means that the MJO modulation in the upper tropospheric O_3 has a lead time of ~10 days relative to that in the lower tropospheric O_3. The observed phase difference at different altitudes is consistent with the observations made by Southern Hemisphere Additional

Table 2. WOUDC Stations (Identification Numbers) Selected for the MJO Analysis[a]

Europe (Box 1)	Japan (Box 2)
35, 40, 43, 53, 68, 96, 99, 100, 174, 213, 261, 262, 279, 284, 305, 308, 312, 316, 318, 331, 346	12, 14, 190, 252, 326, 332

[a]Data acquired only between 2001 and 2010 are used.

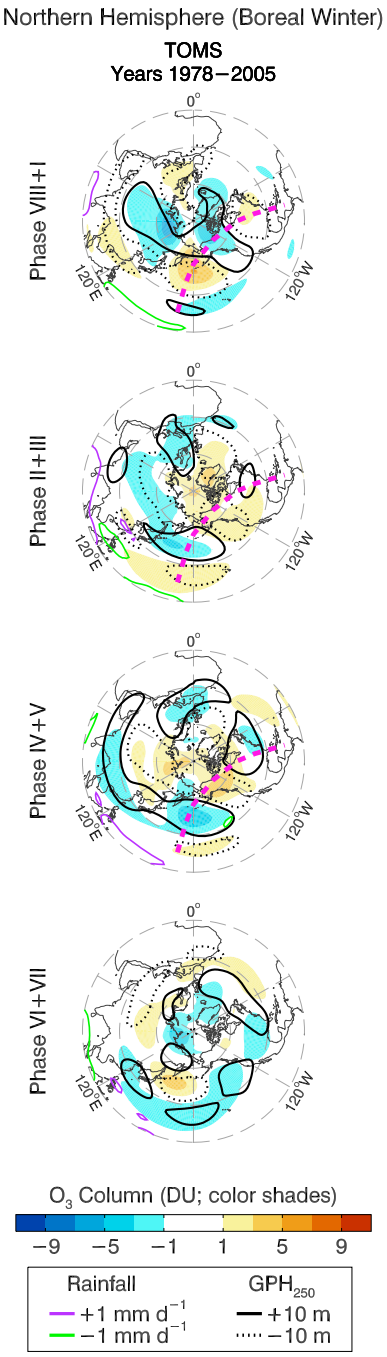

Figure 6. Same as Figure 3 but for TOMS TCO.

Ozonesondes over Fiji (178.40°E, 18.13°S) [*Li et al.*, 2012]. *Li et al.* [2012, Figure 9c] showed that there is a vertical tilt in the MJO-related O_3 anomaly over Fiji, where the O_3 anomaly attains a maximum in Phase 3 at ~150 hPa, while it attains a maximum in Phase 5 at ~40 hPa. Thus, the vertical structure may inform a vertical propagation of the MJO in the extratropical region near the tropopause.

[26] Similarly, over Japan (Figure 5e), the MJO anomalies of WOUDC TCO, MLS PCO, and OMI TCO attain maxima of +1.5 DU in Phase 1 and minima of −1 DU around Phase 5 or 6. Note that the MJO amplitude of the OMI TCO over Japan agrees with the other measurements. There is also a phase lead of 2 MJO phases by TES PCO relative to the others. Therefore, the phase difference observed by TES PCO appears to be robust.

3.5. TOMS O_3

[27] To examine whether there are long-term changes in the MJO teleconnection pattern of O_3, we also average the TOMS TCO data acquired during 1 November 1978 to December 14 2005 in the MJO phases defined by the RMM index (Figure 6). The above MJO composites of GPH_{250} corresponding to November 2002 to November 2011 are also plotted in Figure 6 to (1) illustrate the tropopause movement and (2) serve as a proxy of the present-day MJO teleconnection pattern.

[28] The MJO teleconnection pattern of TOMS TCO is similar to those depicted by the recent measurements in Figure 3, except that the MJO amplitude of the TOMS TCO composites is weaker by a factor of ~2, with the strongest signal over the northern Pacific COA of amplitude ±4 DU. Qualitatively, the negative TOMS TCO anomalies from the long-term measurements are associated with the present-day positive GPH_{250} anomalies and vice versa, showing that the MJO teleconnection through tropopause motion also holds for longer atmospheric records. Same as the OMI TCO, note that due to the absence of TOMS observations during polar nights, the signal over the North Pole may not be robust.

[29] The above results suggest that the same mechanism (such as that described in *Ferranti et al.* [1990]) are likely responsible for the MJO teleconnection in O_3 in different periods. Quantitative differences between TOMS TCO anomalies and MLS PCO, TES PCO, and OMI TCO anomalies may be due to interactions with other interannual variability such as the El Niño–Southern Oscillation (ENSO) and the Pacific Decadal Oscillation, which would require more detailed studies on individual effects.

4. Discussion

[30] It is well known that tropical diabatic heating associated with the MJO excites midlatitude planetary waves via barotropic vorticity perturbations, which then move poleward [*Gill*, 1980; *Ferranti et al.*, 1990; *Kiladis et al.*, 2001; *Seo and Son*, 2012]. These wave perturbations are known to influence northern hemispheric weather patterns in both the troposphere and the stratosphere [*Zhou and Miller*, 2005; *Lin and Brunet*, 2009; *Lin et al.*, 2010b; *Weare*, 2010]. Through the Eliassen-Palm flux, *Weare* [2010] found two coexisting pathways through which the planetary waves may propagate into the northern polar stratosphere on an intraseasonal time scale: (1) The wave flux first moves poleward horizontally at lower altitudes near the tropopause (~ 200 hPa) and then injects vertically into the stratosphere in extratropical regions. (2) The wave flux first injects vertically into the lower/middle stratosphere (50–100 hPa) at lower latitudes and then moves poleward. Since we have found a good correlation between the O_3 and GPH_{250} anomalies in almost the whole Northern Hemisphere, our results suggest that Path 1 involving a barotropic propagation at 250 hPa is adequate for explaining the observed MJO modulations in extratropical O_3 in this hemisphere.

[31] A recent model study [*Seo and Son*, 2012] has suggested that the anomalous tropical heating related to the MJO results in the Rossby wave train of wave numbers 2–3 in the northern hemispheric 200 hPa stream function,

which travels from the Warm Pool northward to the northern Pacific and the North America, then turning southward to the equatorial African continent. The spatial structure of such Rossby wave train is typical of the PNA [*Trenberth and Hurrell*, 1994; *Mori and Watanabe*, 2008]. In this way, energy from the Warm Pool can be transported to higher latitudes along the wave train on an intraseasonal time scale. Such teleconnection through Rossby wave trains in GPH is also evident in the O_3 patterns (highlighted by a pink dashed line in Figure 3).

[32] Polar O_3 in the winter hemisphere may be also modulated remotely by tropical influences through the Brewer-Dobson circulation (BDC) as a result of planetary wave perturbations [*Garcia-Herrera et al*., 2006]. The typical turnover time for the BDC is 1–2 years. While the BDC may play a role in the case of ENSO-related changes in polar O_3 [*Soukharev and Hood*, 2006; *Wang et al*., 2011], its effects on the observed intraseasonal variability, if any, have not be studied quantitatively. Global dynamical effects with different time scales ranging from daily to seasonal may also play a role in the teleconnection [*Hudson et al*., 2003; *Garfinkel et al*., 2012]. There may be also contributions from nonteleconnection processes such as the stratospheric and tropospheric exchange over polar regions on the time scale of ~1 month [*Liang et al*., 2009], which will be further examined in our future work.

[33] The peak-to-trough MJO modulations in lower stratospheric O_3 are typically ~20 DU over the Arctic. Such O_3 changes may modify the polar lower stratospheric temperature profile through radiative heating in the presence of sunlight, which may then change O_3 further given the O_3-GPH correlation described above, forming positive feedback. Detailed simulations with comprehensive feedback mechanisms would be essential for studying these subtle but important effects on Arctic O_3 dynamics and photochemistry (e.g., local O_3 levels at the end of the polar night).

5. Summary

[34] Building on our previous studies [*Tian et al*., 2007; *Li et al*., 2012] which demonstrated the MJO's effects in the subtropical O_3 variations, in this study, we study the MJO modulations in O_3 at northern high latitudes during boreal winters. The RMM index [*Wheeler and Hendon*, 2004] is used to divide an MJO cycle into phases that describe the propagation of the tropical MJO convective disturbances from the western equatorial Indian Ocean to the central equatorial Pacific. When MLS PCO, TES PCO, and TOMS TCO are averaged over these MJO phases, dominant anomalous signals are found over the Arctic (Figure 3). These Arctic O_3 anomalies are negatively correlated with the 250 hPa GPH anomalies that are similarly composited using the RMM index. The negative correlation suggests that the Arctic O_3 anomalies are mainly driven by the vertical movement in the upper troposphere/lower stratosphere, which may be related to the propagation of planetary waves generated by the tropical intraseasonal diabatic heating [*Weare*, 2010]. We also noted a possible connection between the observed extratropical MJO modulations in O_3 with PNA [*Seo and Son*, 2012]. Understanding these teleconnection patterns in chemical tracers like O_3 may help monitor and predict air qualities and ultraviolet levels at higher latitudes as a result of tropical influences.

[35] **Acknowledgments.** K.F.L. is grateful to Prof. Simona Bordoni, Prof. Duane E. Waliser, and Dr. Xianan Jiang for their thoughtful comments. K.F.L. and Y.L.Y. were supported by National Aeronautics and Space Administration (NASA) grant JPL-1429248 to the California Institute of Technology. B.J. was supported by National Science Foundation (NSF) award ATM-0840755 to the University of California, Los Angeles. B.L.S. was supported by NSF grant ATM-0934303. Part of this research was carried out at the Jet Propulsion Laboratory, California Institute of Technology, under a contract with NASA. The RMM index was obtained from http://www.cawcr.gov.au/staff/mwheeler/maproom/RMM/RMM1RMM2.74toRealtime.txt.

References

Beer, R. (2006), TES on the Aura mission: Scientific objectives, measurements, and analysis overview, *IEEE Trans. Geosci. Remote Sens.*, *44*, 1102–1105, doi:10.1109/TGRS.2005.863716.

Beer, R., et al. (2001), Tropospheric emission spectrometer for the Earth Observing System's Aura satellite, *Appl. Opt.*, *40*, 2356–2367, doi:10.1364/AO.40.002356.

Boxe, C. S., et al. (2010), Validation of northern latitude Tropospheric Emission Spectrometer stare ozone profiles with ARC-IONS sondes during ARCTAS: Sensitivity, bias and error analysis, *Atmos. Chem. Phys.*, *10*, 9901–9914, doi:10.5194/acp-10-9901-2010.

Cassou, C. (2008), Intraseasonal interaction between the Madden-Julian Oscillation and the North Atlantic Oscillation, *Nature*, *455*, 523–527, doi:10.1038/nature07286.

Dee, D. P., et al. (2011), The ERA-Interim reanalysis: Configuration and performance of the data assimilation system, *Q. J. R. Meteorol. Soc.*, *137*, 553–597, doi:10.1002/qj.828.

Egger, J., and K. Weickmann (2007), Latitude-height structure of the atmospheric angular momentum cycle associated with the Madden-Julian Oscillation, *Mon. Weather Rev.*, *135*, 1564–1575, doi:10.1175/MWR3363.1.

Eldering, A., et al. (2008), Implementation of cloud retrievals for TES atmospheric retrievals: 2. Characterization of cloud top pressure and effective optical depth retrievals, *J. Geophys. Res.*, *113*, D16S37, doi:10.1029/2007JD008858.

Ferranti, L., et al. (1990), Tropical extratropical interaction associated with the 30–60 day oscillation and its impact on medium and extended range prediction, *J. Atmos. Sci.*, *47*, 2177–2199, doi:10.1175/1520-0469(1990)047<2177:TEIAWT>2.0.CO;2.

Fujiwara, M., et al. (1998), Stratosphere-troposphere exchange of ozone associated with the equatorial Kelvin wave as observed with ozonesondes and rawinsondes, *J. Geophys. Res.*, *103*, 19173–19182, doi:10.1029/98JD01419.

Garcia-Herrera, R., et al. (2006), Propagation of ENSO temperature signals into the middle atmosphere: A comparison of two general circulation models and ERA-40 reanalysis data, *J. Geophys. Res.*, *111*, D06101, doi:10.1029/2005JD006061.

Garfinkel, C. I., et al. (2012), Observed connection between stratospheric sudden warmings and the Madden-Julian Oscillation, *Geophys. Res. Lett.*, *39*, L18807, doi:10.1029/2012GL053144.

Gill, A. E. (1980), Some simple solutions for heat-induced tropical circulation, *Q. J. R. Meteorol. Soc.*, *106*, 447–462, doi:10.1002/qj.49710644905.

Hendon, H. H., and M. L. Salby (1994), The life-cycle of the Madden-Julian Oscillation, *J. Atmos. Sci.*, *51*, 2225–2237, doi:10.1175/1520-0469(1994)051<2225:TLCOTM>2.0.CO;2.

Hoinka, K. P. (1998), Statistics of the global tropopause pressure, *Mon. Weather Rev.*, *126*, 3303–3325, doi:10.1175/1520-0493(1998)126<3303:SOTGTP>2.0.CO;2.

Hollingsworth, A., et al. (2008), Toward a monitoring and forecasting system for atmospheric composition: The GEMS Project, *Bull. Am. Meteorol. Soc.*, *89*, 1147–1164, doi:10.1175/2008BAMS2355.1.

Hoskins, B. J., and G. Y. Yang (2000), The equatorial response to higher-latitude forcing, *J. Atmos. Sci.*, *57*, 1197–1213, doi:10.1175/1520-0469(2000)057<1197:TERTHL>2.0.CO;2.

Hudson, R. D., et al. (2003), The total ozone field separated into meteorological regimes. Part I: defining the regimes, *J. Atmos. Sci.*, *60*, 1669–1677, doi:10.1175/1520-0469(2003)060<1669:TTOFSI>2.0.CO;2.

Huffman, G. J., et al. (2007), The TRMM multisatellite precipitation analysis (TMPA): Quasi-global, multiyear, combined-sensor precipitation estimates at fine scales, *J. Hydrometeorol.*, *8*, 38–55, doi:10.1175/JHM560.1.

Jin, F. F., and B. J. Hoskins (1995), The direct response to tropical heating in a baroclinic atmosphere, *J. Atmos. Sci.*, *52*, 307–319, doi:10.1175/1520-0469(1995)052<0307:TDRTTH>2.0.CO;2.

Jones, C., et al. (2004), The Madden-Julian Oscillation and its impact on Northern Hemisphere weather predictability, *Mon. Weather Rev.*, *132*, 1462–1471, doi:10.1175/1520-0493(2004)132<1462:TMOAII>2.0.CO;2.

Jourdain, L., et al. (2007), Tropospheric vertical distribution of tropical Atlantic ozone observed by TES during the northern African biomass burning season, *Geophys. Res. Lett.*, *34*, L04810, doi:10.1029/2006GL028284.

Jung, T., et al. (2010), Diagnosing the origin of extended-range forecast errors, *Mon. Weather Rev.*, *138*, 2434–2446, doi:10.1175/2010MWR3255.1.

Kiladis, G. N., et al. (2001), Aspects of interannual and intraseasonal variability of the tropopause and lower stratosphere, *Q. J. R. Meteorol. Soc.*, *127*, 1961–1983, doi:10.1002/qj.49712757606.

Kim, B. M., et al. (2006), A new look at the midlatitude-MJO teleconnection in the Northern Hemisphere winter, *Q. J. R. Meteorol. Soc.*, *132*, 485–503, doi:10.1256/qj.04.87.

Kroon, M., et al. (2011), Validation of operational ozone profiles from the Ozone Monitoring Instrument, *J. Geophys. Res.*, *116*, D18305, doi:10.1029/2010JD015100.

Kulawik, S. S., et al. (2006), Implementation of cloud retrievals for Tropospheric Emission Spectrometer (TES) atmospheric retrievals: 1. Description and characterization of errors on trace gas retrievals, *J. Geophys. Res.*, *111*, D24204, doi:10.1029/2005JD006733.

Lau, W. K. M., and D. E. Waliser (2011), *Intraseasonal Variability in the Atmosphere-Ocean Climate System*, 2nd ed., 646 pp., Springer, Heidelberg, Germany.

Leith, C. E. (1973), The standard error of time-average estimates of climatic means, *J. Appl. Meteorol.*, *12*, 1066–1069, doi:10.1175/1520-0450(1973)012<1066:TSEOTA>2.0.CO;2.

Levelt, P. F., et al. (2006a), Science objectives of the Ozone Monitoring Instrument, *IEEE Trans. Geosci. Remote Sens.*, *44*, 1199–1208, doi:10.1109/TGRS.2006.872336.

Levelt, P. F., et al. (2006b), The Ozone Monitoring Instrument, *IEEE Trans. Geosci. Remote Sens.*, *44*, 1093–1101, doi:10.1109/TGRS.2006.872333.

Li, K.-F., et al. (2010), Tropical mid-tropospheric CO_2 variability driven by the Madden-Julian Oscillation, *Proc. Natl. Acad. Sci. U. S. A.*, *107*, 19171–19175, doi:10.1073/pnas.1008222107.

Li, K.-F., et al. (2012), Vertical structure of MJO-related subtropical ozone variations from MLS, TES, and SHADOZ data, *Atmos. Chem. Phys.*, *12*, 425–436, doi:10.5194/acp-12-425-2012.

Liang, Q., et al. (2009), The governing processes and timescales of stratosphere-to-troposphere transport and its contribution to ozone in the Arctic troposphere, *Atmos. Chem. Phys.*, *9*, 3011–3025, doi:10.5194/acp-9-3011-2009.

Lin, H., and G. Brunet (2009), The influence of the Madden-Julian Oscillation on Canadian wintertime surface air temperature, *Mon. Weather Rev.*, *137*, 2250–2262, doi:10.1175/2009MWR2831.1.

Lin, H., et al. (2009), An observed connection between the North Atlantic Oscillation and the Madden-Julian Oscillation, *J. Clim.*, *22*, 364–380, doi:10.1175/2008JCLI2515.1.

Lin, H., et al. (2010a), Impact of the Madden-Julian Oscillation on the intraseasonal forecast skill of the North Atlantic Oscillation, *Geophys. Res. Lett.*, *37*, L19803, doi:10.1029/2010GL044315.

Lin, H., et al. (2010b), Impact of the Madden-Julian Oscillation on wintertime precipitation in Canada, *Mon. Weather Rev.*, *138*, 3822–3839, doi:10.1175/2010MWR3363.1.

Liu, C. X., et al. (2009), A Madden-Julian Oscillation-triggered record ozone minimum over the Tibetan Plateau in December 2003 and its association with stratospheric "low-ozone pockets", *Geophys. Res. Lett.*, *36*, L15830, doi:10.1029/2009GL039025.

Livesey, N. J., et al. (2011), EOS Aura MLS Version 3.3 Level 2 Data Quality and Description Document, *Tech. Rep. JPL D-33509*, 156 pp., Jet Propul. Lab., Pasadena, Calif. [Available at http://mls.jpl.nasa.gov/data/v3-3_data_quality_document.pdf.]

Madden, R. A., and P. R. Julian (1971), Detection of a 40–50 day oscillation in zonal wind in tropical Pacific, *J. Atmos. Sci.*, *28*, 702–708, doi:10.1175/1520-0469(1971)028<0702:DOADOI>2.0.CO;2.

Madden, R. A., and P. R. Julian (1972), Description of global-scale circulation cells in tropics with a 40–50 day period, *J. Atmos. Sci.*, *29*, 1109–1123, doi:10.1175/1520-0469(1972)029<1109:DOGSCC>2.0.CO;2.

Mori, M., and M. Watanabe (2008), Growth and triggering mechanisms of the PNA: A MJO-PNA coherence, *J. Meteorol. Soc. Jpn.*, *86*, 213–236, doi:10.2151/JMSJ.86.213.

Pan, L. L., and T. Li (2008), Interactions between the tropical ISO and midlatitude low-frequency flow, *Clim. Dyn.*, *31*, 375–388, doi:10.1007/s00382-007-0272-7.

Roundy, P. E., and L. M. Gribble-Verhagen (2010), Variations in the flow of the global atmosphere associated with a composite convectively coupled oceanic Kelvin wave, *J. Clim.*, *23*, 4192–4201, doi:10.1175/2010JCLI3630.1.

Seo, K. H., and S. W. Son (2012), The global atmospheric circulation response to tropical diabatic heating associated with the Madden-Julian Oscillation during northern winter, *J. Atmos. Sci.*, *69*, 79–96, doi:10.1175/2011JAS3686.1.

Soukharev, B. E., and L. L. Hood (2006), Solar cycle variation of stratospheric ozone: Multiple regression analysis of long-term satellite data sets and comparisons with models, *J. Geophys. Res.*, *111*, D20314, doi:10.1029/2006JD007107.

Tian, B., and D. E. Waliser (2011), Chemical and biological impacts, in *Intraseasonal Variability of the Atmosphere-Ocean System*, edited by K.-M. Lau and D. E. Waliser, chap. 18, Springer, Heidelberg, Germany.

Tian, B., et al. (2006), Vertical moist thermodynamic structure and spatial-temporal evolution of the MJO in AIRS observations, *J. Atmos. Sci.*, *63*, 2462–2485, doi:10.1175/JAS3782.1.

Tian, B., et al. (2007), Intraseasonal variations of the tropical total ozone and their connection to the Madden-Julian Oscillation, *Geophys. Res. Lett.*, *34*, L08704, doi:10.1029/2007GL029451.

Tian, B., et al. (2008), Does the Madden-Julian Oscillation influence aerosol variability?, *J. Geophys. Res.*, *113*, D12215, doi:10.1029/2007JD009372.

Tian, B., et al. (2010), Vertical moist thermodynamic structure of the Madden-Julian Oscillation in atmospheric infrared sounder retrievals: An update and a comparison to ECMWF Interim Re-Analysis, *Mon. Weather Rev.*, *138*, 4576–4582, doi:10.1175/2010MWR3486.1.

Tian, B., et al. (2011), Modulation of Atlantic aerosols by the Madden-Julian Oscillation, *J. Geophys. Res.*, *116*, D15108, doi:10.1029/2010JD015201.

Trenberth, K. E., and J. W. Hurrell (1994), Decadal atmosphere-ocean variations in the Pacific, *Clim. Dyn.*, *9*, 303–319, doi:10.1007/BF00204745.

Virts, K. S., et al. (2011), Daily and intraseasonal relationships between lightning and NO_2 over the Maritime Continent, *Geophys. Res. Lett.*, *38*, L19803, doi:10.1029/2011GL048578.

Vitart, F., and F. Molteni (2010), Simulation of the Madden-Julian Oscillation and its teleconnections in the ECMWF forecast system, *Q. J. R. Meteorol. Soc.*, *136*, 842–855, doi:10.1002/qj.623.

Waliser, D., et al. (2009), MJO Simulation Diagnostics, *J. Clim.*, *22*, 3006–3030, doi:10.1175/2008JCLI2731.1.

Wallace, J. M., and D. S. Gutzler (1981), Teleconnections in the geopotential height field during the Northern Hemisphere winter, *Mon. Weather Rev.*, *109*, 784–812, doi:10.1175/1520-0493(1981)109<0784:TITGHF>2.0.CO;2.

Wang, J., et al. (2011), El Niño–Southern Oscillation in tropical and midlatitude column ozone, *J. Atmos. Sci.*, *68*, 1911–1921, doi:10.1175/JAS-D-11-045.1.

Waters, J. W., et al. (2006), The Earth observing system microwave limb sounder (EOS MLS) on the Aura satellite, *IEEE Trans. Geosci. Remote Sens.*, *44*, 1075–1092, doi:10.1109/TGRS.2006.873771.

Weare, B. C. (2010), Madden-Julian Oscillation in the tropical stratosphere, *J. Geophys. Res.*, *115*, D17113, doi:10.1029/2009JD013748.

Weare, B. C., et al. (2012), Madden-Julian Oscillation in a climate model with a well-resolved stratosphere, *J. Geophys. Res.*, *117*, D01103, doi:10.1029/2011JD016247.

Weickmann, K., and E. Berry (2009), The tropical Madden-Julian Oscillation and the Global Wind Oscillation, *Mon. Weather Rev.*, *137*, 1601–1614, doi:10.1175/2008MWR2686.1.

Wheeler, M. C., and H. H. Hendon (2004), An all-season real-time multivariate MJO index: Development of an index for monitoring and prediction, *Mon. Weather Rev.*, *132*, 1917–1932, doi:10.1175/1520-0493(2004)132<1917:AARMMI>2.0.CO;2.

Wong, S., and A. E. Dessler (2007), Regulation of H_2O and CO in tropical tropopause layer by the Madden-Julian Oscillation, *J. Geophys. Res.*, *112*, D14305, doi:10.1029/2006JD007940.

Worden, H. M., et al. (2007), Comparisons of Tropospheric Emission Spectrometer (TES) ozone profiles to ozonesondes: Methods and initial results, *J. Geophys. Res.*, *112*, D03309, doi:10.1029/2006JD007258.

Yoo, C., et al. (2011), The impact of the Madden-Julian Oscillation trend on the Arctic amplification of surface air temperature during the 1979–2008 boreal winter, *Geophys. Res. Lett.*, *38*, L24804, doi:10.1029/2011GL049881.

Yoo, C., et al. (2012), Mechanisms of arctic surface air temperature change in response to the Madden-Julian Oscillation, *J. Clim.*, *25*, 5777–5790, doi:10.1175/JCLI-D-11-00566.1.

Zhang, C. D. (2005), Madden-Julian Oscillation, *Rev. Geophys.*, *43*, RG2003, doi:10.1029/2004RG000158.

Zhou, S. T., and A. J. Miller (2005), The interaction of the Madden-Julian Oscillation and the Arctic Oscillation, *J. Clim.*, *18*, 143–159, doi:10.1175/JCLI3251.1.

Ziemke, J. R., and S. Chandra (2003), A Madden-Julian Oscillation in tropospheric ozone, *Geophys. Res. Lett.*, *30*, 2182, doi:10.1029/2003GL018523.

Ziemke, J. R., et al. (2007), Intra-seasonal variability in tropospheric ozone and water vapor in the tropics, *Geophys. Res. Lett.*, *34*, L17804, doi:10.1029/2007GL030965.